nature biotechnology

A DNA nanorobot functions as a cancer therapeutic in response to a molecular trigger *in vivo*

Suping Li[1,2,10], Qiao Jiang[1,10], Shaoli Liu[1,2,10], Yinlong Zhang[1,3,10], Yanhua Tian[1,4], Chen Song[1], Jing Wang[1], Yiguo Zou[1], Gregory J Anderson[5], Jing-Yan Han[6], Yung Chang[7], Yan Liu[7], Chen Zhang[8], Liang Chen[9], Guangbiao Zhou[8], Guangjun Nie[1,2], Hao Yan[7], Baoquan Ding[1,2] & Yuliang Zhao[1,2]

Nanoscale robots have potential as intelligent drug delivery systems that respond to molecular triggers[1–4]. Using DNA origami we constructed an autonomous DNA robot programmed to transport payloads and present them specifically in tumors. Our nanorobot is functionalized on the outside with a DNA aptamer that binds nucleolin, a protein specifically expressed on tumor-associated endothelial cells[5], and the blood coagulation protease thrombin within its inner cavity. The nucleolin-targeting aptamer serves both as a targeting domain and as a molecular trigger for the mechanical opening of the DNA nanorobot. The thrombin inside is thus exposed and activates coagulation at the tumor site. Using tumor-bearing mouse models, we demonstrate that intravenously injected DNA nanorobots deliver thrombin specifically to tumor-associated blood vessels and induce intravascular thrombosis, resulting in tumor necrosis and inhibition of tumor growth. The nanorobot proved safe and immunologically inert in mice and Bama miniature pigs. Our data show that DNA nanorobots represent a promising strategy for precise drug delivery in cancer therapy.

DNA molecules have been shown to be excellent substrates for the design and construction of mechanical molecular devices that sense, actuate and exert functions when exposed to external signals[1]. DNA-based robotics has been used as imaging probes[2,6,7] and cargo delivery vehicles[3,7,8] in cultured cells[2,3], *Caenorhabditis elegans*[7] and insects[4]. However, robotic DNA machines serving as intelligent vehicles for *in vivo* targeting drug delivery and controlled release in mammals have—to our knowledge—not yet been described.

Selective occlusion of tumor blood vessels, to deprive tumors of nutrients and oxygen and start an avalanche of tumor cell death, is an attractive strategy for combating cancer[9–13]. Vascular occlusion can exert its effects within hours following the rapid induction of thrombus formation in tumor vessels, and carries a decreased risk of resistance development. Moreover, vascular occlusion is a strategy that can be used for many types of cancer, as all solid tumor-feeding vessels are essentially the same[11,12].

The coagulation protease thrombin regulates platelet aggregation by activating platelets and converting circulating fibrinogen to fibrin[14], ultimately leading to obstructive thrombosis. Naked thrombin is short-lived in the circulation and induces coagulation events indiscriminately, and has not been used in cancer treatment. For therapeutic use, it is therefore critical to precisely deliver thrombin solely to tumor sites in a highly controlled manner to minimize its effects in healthy tissues.

DNA origami is a method that enables the rational design and production of DNA nanostructures with controlled size, shape and spatial addressability[15–18], producing functional platforms for biological applications[3,4,6,19–22]. Using DNA origami, we constructed a DNA nanorobotic system to overcome the challenges associated with thrombin delivery to tumors. Our nanorobot protects thrombin until exposure is triggered by the interaction with the tumor vessel marker nucleolin. Using the thrombin-loaded nanorobot, we demonstrate on-site tumor blood vessel infarction and targeted cancer treatment *in vivo*.

To deliver active thrombin solely to tumor sites in a highly controlled way, we developed a DNA nanorobotic system based on a self-assembled origami nanotube with multiple functional elements (**Fig. 1a** and **Supplementary Table 1**). A rectangular DNA origami sheet, measuring 90 nm × 60 nm × 2 nm (**Supplementary Fig. 1**), was first prepared by assembling an M13 bacteriophage genome DNA strand and multiple staple strands. For thrombin loading, capture strands with poly-A sequences were extended at four designated locations on the surface of each DNA origami sheet (**Supplementary Figs. 2** and **3**). We synthesized the thrombin–DNA conjugates by attaching thiolated poly-T oligonucleotides to thrombin molecules through a

[1]CAS Key Laboratory for Biomedical Effects of Nanomaterials & Nanosafety, CAS Key Laboratory of Nanosystem and Hierarchical Fabrication, CAS Center for Excellence in Nanoscience, National Center for Nanoscience and Technology, China, Beijing, China. [2]University of Chinese Academy of Sciences, Beijing, China. [3]College of Pharmaceutical Science, Jilin University, Changchun, China. [4]Peking-Tsinghua Center for Life Sciences, Academy for Advanced Interdisciplinary Studies, Peking University, Beijing, China. [5]QIMR Berghofer Medical Research Institute, Brisbane, Queensland, Australia. [6]Department of Integration of Chinese and Western Medicine, School of Basic Medical Sciences, Peking University, Beijing, China. [7]School of Molecular Sciences, Center for Molecular Design and Biomimetics; School of Life Sciences, Center for Immunotherapy, Vaccines, and Virotherapy at the Biodesign Institute, Arizona State University, Tempe, Arizona, USA. [8]Institute of Zoology, Chinese Academy of Sciences, Beijing, China. [9]Institute of Life and Health Engineering, College of Life Science and Technology, Jinan University, Guangzhou, China. [10]These authors contributed equally to this work. Correspondence should be addressed to G.N. (niegj@nanoctr.cn), H.Y. (hao.yan@asu.edu), B.D. (dingbq@nanoctr.cn) or Yuliang Zhao (zhaoyl@nanoctr.cn).

Received 16 June 2016; accepted 9 January 2018; published online 12 February 2018; doi:10.1038/nbt.4071

cross-linker sulfo-SMCC (sulfosuccinimidyl-4-[*N*-maleimidomethyl]cyclohexane-1-carboxylate; **Supplementary Figs. 4** and **5**), and mixed the conjugates with the DNA origami sheet. The extended poly-A strands on the DNA sheet were then able to hybridize with the poly-T on the conjugates (**Supplementary Fig. 6a**), allowing thrombin molecules to be anchored on the surface of the DNA sheet (**Fig. 1a**). Biological activity assays showed that both the thrombin–DNA conjugates and the thrombin bound to the DNA origami sheet retained their catalytic activity (**Supplementary Fig. 6b**). Atomic force microscopy images demonstrate that more than 70% of the DNA sheets contained four bound thrombin molecules (**Supplementary Figs. 7–9**). Using a Cy5.5-labeling approach for thrombin quantification, the average number of thrombin on each DNA origami sheet was calculated to be 3.8 ± 0.4 (**Supplementary Fig. 10**).

Our hollow tube-shaped DNA nanorobot, with a diameter of ~19 nm and a length of 90 nm (**Fig. 1a** and **Supplementary Fig. 11**), was next formed by fastening the thrombin-loaded DNA origami sheet along the long sides (**Fig. 1a** and **Supplementary Table 2**). The four thrombin molecules, attached to the inner surface of the tubular nanorobot (**Supplementary Fig. 12**), thus became shielded from circulating platelets and plasma fibrinogen. By hybridization of predesigned fastener strands containing DNA aptamers (AS1411)[23], the tube-shaped DNA nanorobot was non-covalently closed along a defined seam (**Fig. 1a** and **Supplementary Fig. 11**). We confirmed the closed and open states of the DNA nanorobot by atomic force microscopy (**Fig. 1b**). The four bright spots on the surface of the origami sheet represent the raised height produced by the thrombin cargo.

We hypothesize that when the fastener strands recognize their targets, in our case nucleolin proteins selectively expressed on the surface of actively proliferating tumor vascular endothelial cells[5], the hybridized duplexes will dissociate to induce reconfiguration of the nanorobot to expose the contained cargo. To test this hypothesis, we first used flow cytometry to examine the nucleolin recognition and dissociation of the DNA fastener strands. The Y-shaped fastener structures (**Supplementary Fig. 13**), each containing a 15-base-pair duplex, were composed of two DNA strands: F50, which contains AS1411 aptamer sequences that are able to specifically bind to nucleolin expressed on the surface of cultured human umbilical vein endothelial cells (HUVECs; **Supplementary Fig. 14**), and Comp15, a strand partially complementary to the AS1411 sequence of F50. As with free F50, the Y-shaped structure containing the 15-bp duplex was able to effectively bind to HUVECs (**Supplementary Fig. 15**), demonstrating that the fastener strands recognize nucleolin on the cell surface.

To determine whether the fasteners can dissociate after binding to recombinant nucleolin or nucleolin-positive HUVECs, we prepared dye-labeled fasteners (5′-fluorescence-labeled F50 and 3′-quencher-labeled Comp15; **Fig. 2a** and **Supplementary Fig. 16**) serving as switchable fluorescent beacons. These beacons emit only a weak fluorescence when hybridized. Upon recognizing recombinant nucleolin or that on the surface of HUVECs, the fasteners are activated: fluorophore-labeled F50 strands switch to the G-quadruplex state[24] and bind to nucleolin, while the quencher-labeled Comp15 is released, resulting in a high fluorescence intensity. Indeed, binding of the labeled fasteners to nucleolin in solution (**Supplementary Fig. 16**) or on the HUVECs (**Fig. 2b**) substantially increased fluorescence signal intensity. For comparison, the other two Y-shaped structures (fully complementary 26-bp duplex of AS1411 sequences or controls lacking any AS1411 sequence) were not activated by HUVECs (**Fig. 2b**). A similar experiment was performed to demonstrate that the binding of nucleolin can open the DNA nanorobots. Six pairs of

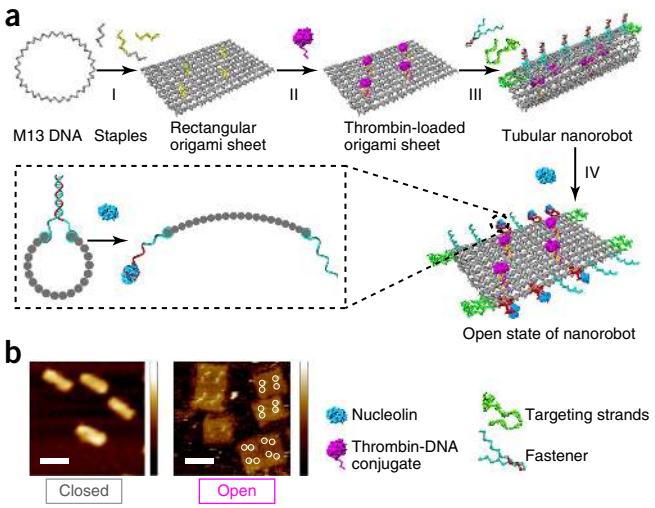

Figure 1 Design and characterization of thrombin-functionalized DNA nanorobot. (**a**) Schematic illustration of the construction of thrombin-loaded nanorobot by DNA origami, and its reconfiguration into a rectangular DNA sheet in response to nucleolin binding. (**a**, **I**) Single-stranded M13 phage genomic DNA is linked by predesigned staple strands, leading to the formation of a rectangular DNA sheet. (**a**, **II**) Thrombin is loaded onto the surface of the DNA sheet structure by hybridization of poly-T oligonucleotides conjugated to thrombin molecules with poly-A sequences that extend from the surface of the DNA sheet. (**a**, **III**) Addition of the fasteners and targeting strands results in the formation of thrombin-loaded, tubular DNA nanorobots with additional targeting aptamers at both ends. (**a**, **IV**) The tube nanocarrier opens in response to the presence of nucleolin to expose the encapsulated thrombin. (**b**) DNA nanorobots were examined by atomic force microscopy (AFM) and representative images of closed (left) and opened states (right) are shown. The four bright spots displayed on the surface of the origami sheet represent the thrombin molecules (thrombin molecules on the four DNA-sheet-thrombin assemblies on the right of open states image are highlighted by white circles). The AFM images are representative of three independent experiments. Scale bars, 100 nm.

Y-shaped fastener structures consisting of 5′-FITC-labeled F50 and 3′-BHQ1-labeled Comp15 were used to close the DNA nanorobot. With the DNA nanorobot in the 'fastened' state, the FITC fluorescence is quenched by BHQ1. Upon opening, the DNA nanorobot is expected to produce a strong increase in fluorescence intensity. The fluorophore–quencher–pair–labeled nanorobot was treated with recombinant nucleolin or nucleolin-positive HUVECs and a substantial increase in fluorescence intensity was observed in both cases, indicating the opening of the nanorobot (**Fig. 2c**,**d** and **Supplementary Fig. 17**). In contrast, starved HUVECs, whose surface nucleolin expression is downregulated (**Supplementary Fig. 18**), did not cause the DNA nanorobot to open (**Fig. 2d**).

We next investigated *in vitro* blood coagulation to determine whether the thrombin-loaded nanorobot (nanorobot-Th) opens in response to the target protein and exposes functional thrombin. When mouse plasma was mixed with nanorobot-Th and HUVECs, it coagulated rapidly, with a fibrin formation time of 82 s, as compared to 176 s when cells were absent and 177 s with cells alone (**Fig. 2e**,**f**). This enhanced coagulation was comparable to the fastener-free, thrombin-loaded DNA origami sheet, indicating a cell-induced opening of the nanotubes. No effect on coagulation time was seen when plasma was added to cells incubated with an empty DNA nanorobot. Further, we found that there was a positive relationship between the rate of plasma coagulation and the concentration of nanorobot-Th added (**Supplementary Fig. 19**). These data demonstrate that the DNA

nanorobot is able to change its structure in response to target cells, and that the exposed thrombin payload can induce coagulation.

We examined the ability of the DNA nanorobot to remain bound to surface nucleolin-positive cells. To ensure a maximal targeting effect, we decorated the staple strands of the origami structures with additional targeting aptamer sequences at both ends of the tubes (**Fig. 1a** and **Supplementary Table 2**). To visualize the endothelial cell targeting, we modified the staple strands of the central region of the origami structure to contain a single-strand extension (imaging strand) that can hybridize to Alexa 594–labeled oligonucleotides (**Supplementary Fig. 2**). The results of confocal microscopy and flow cytometry assays suggest that eight additional AS1411 strands at both ends (four for each end) elicited a maximal binding to cultured HUVECs (**Supplementary Fig. 20**). Time-course data further revealed a rapid association of such nanorobots to HUVECs, with maximal binding attained within 1 h and a cell surface dwell time of at least 6 h (**Fig. 2g**). In contrast, the bare nanotubes rolled without the targeting aptamer strands (referred to as 'nontargeted nanotubes') did not bind to the surface of HUVECs. The binding of a nanorobot was dependent upon cell surface nucleolin as the presence of an anti-nucleolin antibody abolished the binding. In addition, most of nanorobot-Th maintained their nanostructures over a 24-h period in the presence of bovine serum albumin (BSA) or fetal bovine serum (FBS) (**Supplementary Fig. 21**), suggesting a potential high stability in blood circulation.

To investigate tumor vessel targeting of the nanorobot *in vivo*, we performed fluorescence imaging on mice bearing orthotopic tumors. Human breast cancer cells (MDA-MB-231) were injected into the mammary fat pads of BALB/c nude mice. Mice displaying tumor volumes around 100 mm^3 were intravenously injected (i.v.) with Cy5.5-labled DNA nanorobots. The nanorobots progressively accumulated in the tumor, reaching a maximal accumulation at 8 h after injection (**Fig. 3a**,**b**). Substantial differences were observed between the targeted nanorobots and nontargeted nanotubes in the tumor signal intensities (**Supplementary Fig. 22a**–**c**). Quantitative analysis revealed that the targeted nanorobots accumulated in the tumor about seven times more efficiently than the nontargeted nanotubes 8 h after injection (**Supplementary Fig. 22b**). This result indicates that the aptamer-conjugated nanorobots were able to target tumors *in vivo*. To further determine whether the nanorobot indeed targets the nucleolin-positive tumor endothelium, we stained tumor sections for the endothelial cell marker CD34 after administration of FITC-labeled nanorobots. The nanorobots effectively bound to the tumor vascular endothelium, as evidenced by their co-localization with CD34 (**Fig. 3c**).

We also examined the time-dependent organ distribution and clearance of the DNA nanorobots and controls after intravenous injection (**Supplementary Fig. 22c**). Shortly (1 h) after injection, the DNA nanostructures accumulated in the liver, presumably having been captured by the mononuclear phagocyte system. In time, the intensity of the liver fluorescence decreased, suggesting that the nanostructures not entrapped by the tumor may be degraded following phagocytosis, as generally observed for nanoscale delivery vehicles[25]. At 24 h post-injection, little fluorescence was observable in the major organs and the fluorescence in the tumor also decreased substantially demonstrating the successful clearance or degradation of the material.

We next investigated whether the nanorobot would expose thrombin after targeted delivery to tumor-associated blood vessels thereby inducing thrombosis, resulting in vessel infarction and tumor necrosis (**Fig. 3d**). First, we assessed the tumor vessels for targeted

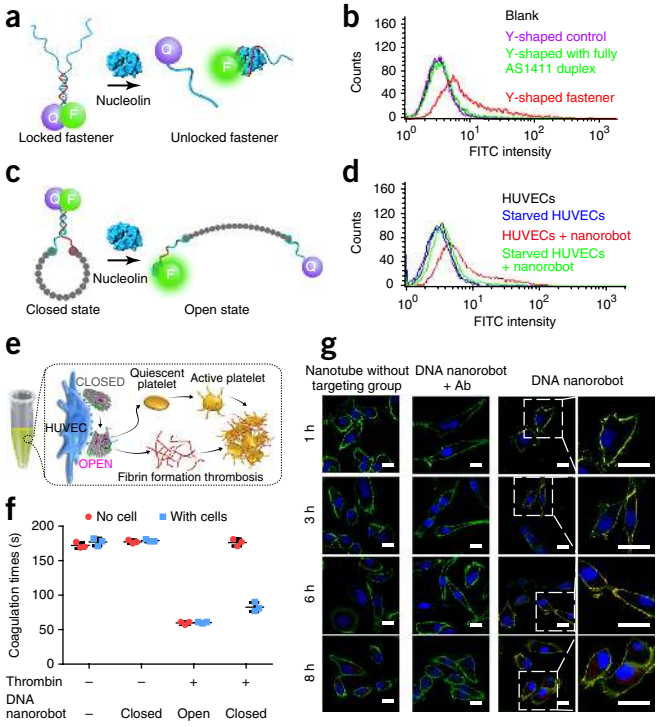

Figure 2 Analysis of DNA nanorobot-triggered activation and endothelial cell targeting. (**a**) Scheme of Y-shaped fastener strands and dissociation in response to nucleolin recognition. F and Q represent fluorescent and quencher molecules, respectively. The 15-bp partially complementary duplex switches to the G-quadruplex state to form an AS1411–nucleolin complex in response to the nucleolin target protein. (**b**) Flow cytometry histograms showing Y-shaped fastener dissociation after a 2-h incubation with HUVECs, as measured by cell labeling with FITC-labeled F50 containing AS1411 sequences. HUVECs treated with fasteners of a partially (15-bp, red line) and fully complementary (26-bp, green line) AS1411 duplex are shown. Cells incubated with control Y-shapes without the AS1411 portion are represented by the purple line while unstained cells are the black line. The results are representative of three independent experiments. (**c**) Scheme of fluorophore–quencher pair-fastened DNA nanorobot and reconfiguration in response to nucleolin recognition. (**d**) Flow cytometry histograms showing fastened DNA nanorobot triggered reconfiguration by HUVECs after a 2-h incubation, resulting in enhanced fluorescence intensity. The starved HUVECs, a state in which surface nucleolin expression is downregulated, cannot open the DNA nanorobot. The results are representative of three independent experiments. (**e**) Schematic representation of the mechanism of action of nanorobot-Th in plasma in the presence of vascular endothelial cells. Thrombin molecules are arranged at four designated locations inside the nanorobot in an inactive state. The closed nanorobot is mixed with mouse plasma and HUVECs to mimic the tumor-associated microenvironment. The nanorobot binds to HUVECs by recognizing the cell surface target protein, nucleolin, and the tube subsequently opens to expose the encapsulated thrombin to induce thrombosis. (**f**) Induction of coagulation by cell-bound nanorobot-Th. Error bars represent the mean ± s.d. of three independent experiments. (**g**) Confocal microscopy showing the targeting of nanorobot to nucleolin-positive HUVECs. Alexa 594-labeled nanorobot (red) with additional targeting aptamer strands at both ends binds to the cells in the absence of an antibody to nucleolin, while those lacking targeting groups do not bind. The perinuclear accumulation of red fluorescence after an 8-h incubation indicates internalization of the nanostructures. Images were acquired at 1, 3, 6 or 8 h after incubation of the cells with nanorobot or nanotubes. Nucleus and plasma membrane were stained with DAPI (blue) and DiO (green), respectively. The colocalization of nanostructures with cell membranes appears in yellow (merge). The fluorescence images are representative of three independent experiments; additional high-magnification images are shown of the insets for the nanorobot-treated cells. Scale bars, 20 μm.

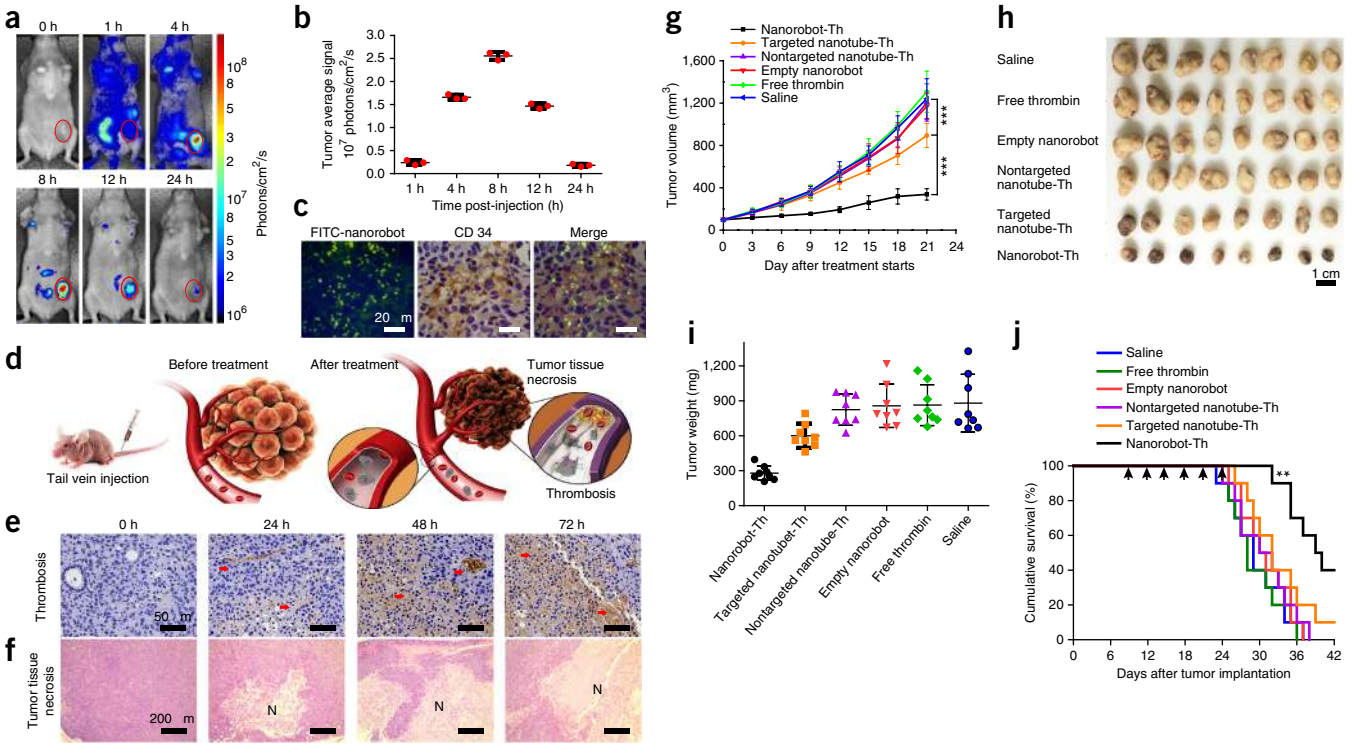

Figure 3 DNA nanorobots target tumors, induce thrombosis in tumor vessels and inhibit tumor growth *in vivo*. (**a**) Optical imaging of an MDA-MB-231 mouse bearing a human breast tumor before and after intravenous injection of Cy5.5-labeled nanorobot. A high-intensity fluorescent signal was detected only in the tumor region of mice 8 h after injection. 0 h = before injection. The images are representative of three independent experiments. (**b**) *In vivo* fluorescence intensity at the tumor sites was measured at the indicated time points after administration of the nanorobots. Error bars represent the mean ± s.d. of three independent experiments. (**c**) FITC-labeled nanorobots were injected intravenously into mice bearing MDA-MB-231 tumors. Tumors were harvested 8 h later, and tumor sections were stained with an anti-CD34 antibody and examined by confocal microscopy. The nanorobot (green) appears in the blood vessel-rich regions (anti-CD34; brown). Nuclei are indicated in blue. The images are representative of three independent experiments. Scale bars, 20 μm. (**d**) Schematic representation of the therapeutic mechanism of nanorobot-Th within tumor vessels. DNA nanorobot-Th was administrated to breast tumor xenografted mice by tail vein injection and targeted tumor-associated vessels to deliver thrombin. The nanorobot-Th binds to the vascular endothelium by recognizing nucleolin and opens to expose the encapsulated thrombin, which induces localized thromboses, tumor infarction and cell necrosis. (**e**) MDA-MB-231 tumors harvested before and 24, 48 or 72 h after administration of nanorobot-Th were immunostained for CD41 (activated platelets) to detect thrombosis (brown, indicated by red arrows). The images are representative of three independent experiments. Scale bars, 50 μm. (**f**) Tumors harvested before and 24, 48 or 72 h after treatment with nanorobot-Th were stained with H&E. Necrotic tissues are denoted by N. Scale bars, 200 μm. Data are representative of three independent experiments. (**g**–**i**) MDA-MB-231 tumor-bearing mice were treated on day 0 with saline, free thrombin, targeted empty nanorobot, nontargeted nanotube-Th, targeted nanotube-Th or nanorobot-Th. Tumor volumes up to day 21 (**g**, $n = 8$ biologically independent, nanorobot-Th vs. targeted nanotube-Th, $P = 0.00016$; targeted nanotube-Th vs. saline, $P = 0.00031$). Representative pictures of the tumors (**h**) and average tumor weights (**i**, error bars represent the mean ± s.d. of 8 tumors) of the indicated groups of mice. (**j**) Cumulative survival of MDA-MB-231 tumor-bearing mice ($n = 10$) compared using Mantel–Cox Log-rank test, $P = 0.0048$. Black arrows indicate the injection time points.

thrombosis after administration of nanorobot-Th (**Fig. 3e**). Blood vessels in the tumor region were occluded within 24 h, as demonstrated by the detection of widespread platelet aggregates by means of an antibody specific for CD41 on the activated platelet surface. After 48 h, there was advanced thrombosis, and by 72 h, dense thrombi in all tumor vessels were observed. In contrast, there was no visible thrombosis in the tumor vessels of mice after administration of saline or equivalent doses of free thrombin, targeted empty nanorobots or nontargeted thrombin-loaded nanotubes (nanotube-Th) for up to 72 h (**Supplementary Fig. 23a**). A weak thrombotic activity was observed with targeted nanotube-Th (**Supplementary Fig. 23a**, 72 h), which has a similar tumor targeting ability as nanorobot-Th (**Supplementary Fig. 22**), but was unable to open after binding to nucleolin. It is possible that passive degradation of targeted nanotubes within tumors results in exposure of a portion of the active thrombin to induce thrombosis. Neither thrombi nor histological abnormalities were found in the heart, liver, lung or kidney from the tumor-bearing mice 72 h after administration of nanorobot-Th (**Supplementary Fig. 23b**), verifying that thrombosis was specific to the tumor vasculature. H&E staining revealed advanced tumor necrosis over time in the nanorobot-Th treated group (**Fig. 3f**), and limited necrosis was also found in the targeted nanotube-Th-treated group (**Supplementary Fig. 23c**), whereas no necrosis was observed in any other group.

To investigate the therapeutic potential of nanorobot-Th, we randomly sorted MDA-MB231 tumor-bearing nude mice and treated each group through tail vein injection as follows: saline, free thrombin, targeted empty nanorobot, nontargeted nanotube-Th, targeted nanotube-Th or nanorobot-Th. Injections were carried out six times at intervals of 3 d. Mice treated with saline, free thrombin, empty nanorobots or nontargeted nanotube-Th formed fast-growing tumors (**Fig. 3g**–**i**). In contrast, tumors grew substantially more slowly in mice treated with nanorobot-Th, indicating a therapeutic effect in inhibiting tumor growth. This correlated with a significant increase in animal survival (**Fig. 3j**). The median survival time for mice treated with saline was 29 d, and treatment with free thrombin, empty nanorobots or nontargeted nanotube-Th had no significant

effect on this time. Nanorobot-Th treatment increased this survival to 39 d. Tumors in mice receiving targeted nanotube-Th grew slightly slower than did tumors in mice receiving saline, free thrombin, empty nanorobots or nontargeted nanotube-Th (**Fig. 3g–i**). Treatment with targeted nanotube-Th slightly increased animal survival to 32 d (**Fig. 3j**). The weak inhibitory effect presumably correlates with its modest thrombogenic activity in tumor vessels, as evidenced in tumor sections (**Supplementary Fig. 23a**). The nanorobot-Th proved to be even more effective in a B16-F10 melanoma mouse model (**Fig. 4a**,**b**), in which three out of eight of the mice receiving nanorobot-Th showed complete regression of the tumors. The median survival time of the mice was extended from 20.5 to 45 d compared to the saline group. This higher efficacy was likely a consequence of the higher grade of vascularization of melanoma tumors. Nanorobot-Th treatment also effectively prevented the occurrence of melanoma metastases in the liver (**Fig. 4c**,**d**), which can likely be attributed to the inhibition of primary tumor progression or to the regression of vascularized metastases.

We next investigated the antitumor activity of nanorobot in less vascularized tumors. Mice bearing subcutaneous xenografts of human ovarian cancer cells, SK-OV3, which have been reported to be poorly vascularized[26] and have a relatively low permeability and retention for Evans blue (**Fig. 4e**), exhibited significantly restrained tumor growth after treatment with nanorobot-Th, compared to mice treated with saline, free thrombin or control nanostructures (**Fig. 4f**,**g**). Nanorobot-Th treatment also significantly prolonged the survival of animals with xenografts (**Fig. 4h**). Although in this case the inhibitory efficiency of the DNA nanorobot was not as remarkable as in the melanomas, the results nonetheless show that limited tumor permeability does not prevent the nanorobot from exerting antitumor activity. Moreover,

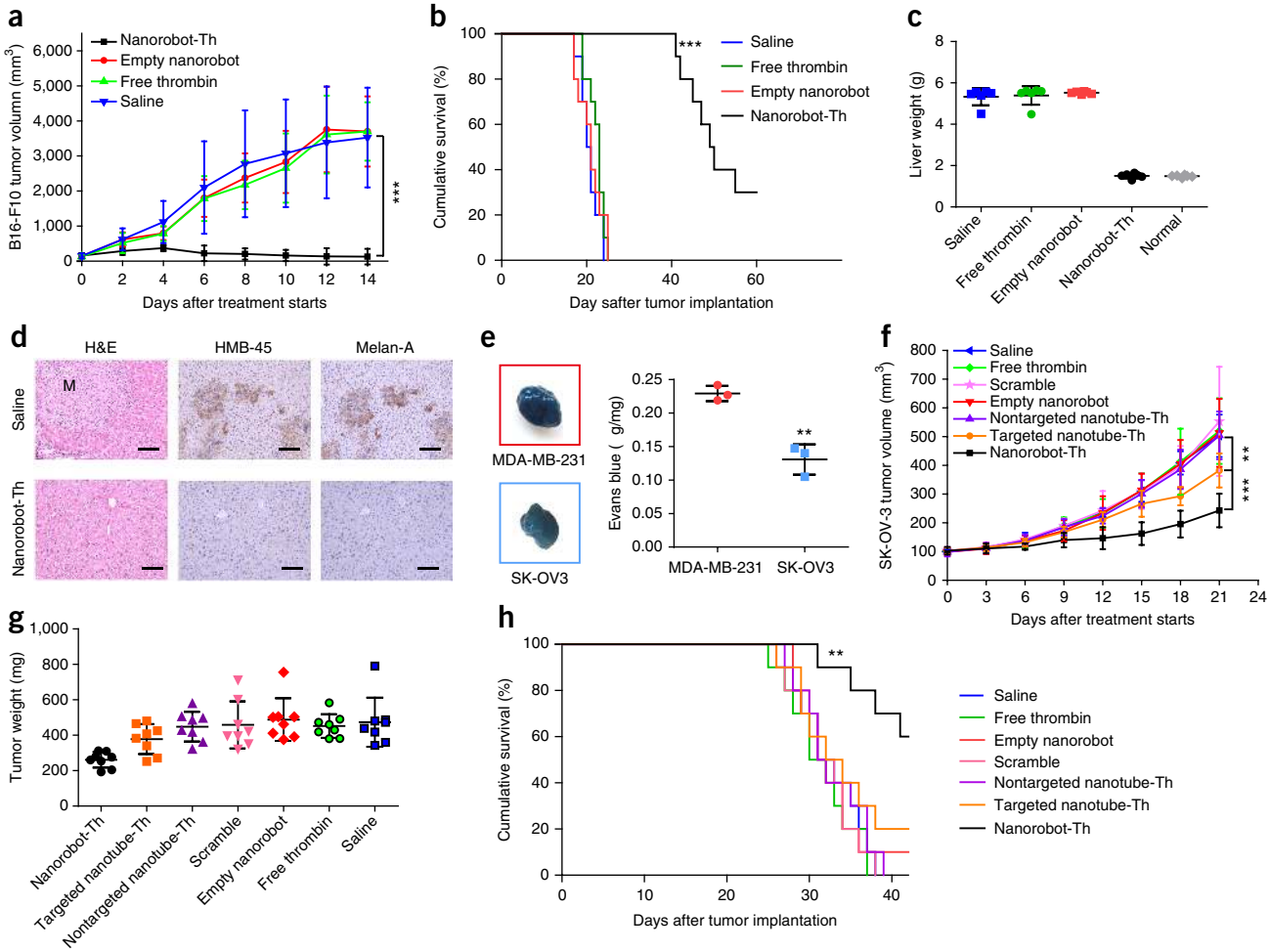

Figure 4 Treatment with nanorobot-Th inhibits the growth of melanoma and poorly vascularized SK-OV3 ovarian cancer. (**a**,**b**) B16-F10 cells were injected subcutaneously into the flanks of C57BL/6J mice. Tumor volumes up to day 14 (**a**, $P = 0.000011$) and cumulative survival (**b**, $P = 0.0003$, Mantel–Cox Log-rank test) of mice were noted ($n = 10$). (**c**,**d**) Melanoma metastases. Liver weight after eight treatments; the results are representative of six independent experiments (**c**). H&E staining of liver sections (**d**, left). Staining of liver sections for the melanoma markers HMB-45L (**d**, middle, brown) and Melan-A (**d**, right, brown), and nuclei are indicated in blue. The images are representative of three independent experiments. Scale bars, 50 µm. (**e**) Mice bearing ~250 mm^3 SK-OV3 and MDA-MB-231 tumors were injected intravenously with 100 µl 5% Evans blue. After 3 h, the tumors were removed and photographed (left). Evans blue was extracted by treating the tumor tissues with formamide for 3 d and quantified using a UV-Vis spectrophotometer (620 nm; right). Data are shown as the mean ± s.d. The results are representative of three independent experiments. $P = 0.003$. (**f**–**h**) SK-OV3 tumor volumes up to day 21 (**f**, $n = 8$ biologically independent, error bars represent the mean ± s.d.; nanorobot-Th vs. targeted nanotube-Th, $P = 0.0011$; targeted nanotube-Th vs. saline, $P = 0.0047$). Tumors excised at day 21 were weighed (**g**, $n = 8$ biologically independent, error bars represent the mean ± s.d.). (**h**) Cumulative survival of SK-OV3 tumor-bearing mice ($n = 10$, error bars represent the mean ± s.d.; Mantel–Cox Log-rank test, $P = 0.0099$).

encouraging therapeutic results were also observed in a doxycycline-inducible Kras mutation lung cancer model, generated using transgenic *TetO-Kras^{G12D}* mice[27], which faithfully recapitulates the clinical course of human lung cancer. Magnetic resonance imaging (MRI) was used to assess tumor extent before and after 1- and 2-week periods of treatment with nanorobot-Th once every 3 d. The nanorobot-Th clearly was beneficial in the *TetO-Kras^{G12D}* mutant mice, who showed a significant inhibition of tumor progression during the 2 weeks of observation, as assessed by MRI (**Supplementary Fig. 24a**,**b**) and wet lung weight measurement (**Supplementary Fig. 24c**). H&E staining revealed that the tumor regions were riddled with intratumoral spaces after the 2-week treatment with nanorobot-Th (**Supplementary Fig. 24d**), indicating that tumor growth was retarded. H&E-stained sections also showed thickening of alveolar wall and fibrosis, suggesting a consequential remodeling of the tumor tissues into normal lung tissues. In contrast, the mice treated with saline, thrombin or the nontargeting nanotube-Th displayed rapid tumor growth, with an ~100% increase in tumor growth during this period of treatment. Collectively, these data show that our targeted thrombin delivery system based on a reconfigurable DNA nanostructure exhibits promising *in vivo* antitumor efficacy, and is applicable to tumors of diverse levels of vascularization.

Finally, we carried out comprehensive *in vitro* and *in vivo* safety assessments of the DNA nanorobotic system. We first found that doses of free thrombin equivalent to those used *in vivo* in the nanorobot system elicited no observable thrombi in the cerebral microcirculation in non-tumor-bearing healthy mice. However, transient, reversible microthrombi were apparent in much higher concentrations (**Supplementary Fig. 25a** and **Supplementary Table 2**). As for the DNA nanorobots themselves, no significant changes were observed in blood coagulation parameters (including platelet activity, plasma thrombin and fibrin concentrations, and circulating platelet numbers) after treatment with nanorobot-Th in the non-tumor-bearing mice compared to the control group (**Supplementary Fig. 25b**–**e**). There were also no observable cerebral microthrombi in mice 24 h after injection of nanorobot-Th (**Supplementary Fig. 25f**). In addition, nanorobot-Th treatment had no significant impact on cytokine levels (IL-6, IP-10, TNF-α and IFN-α) (**Supplementary Fig. 26**), suggesting the DNA nanorobot system is immunologically inert, which is in accordance with previous observations[8,21,28]. The nanorobot-Th also did not cause any observable cytotoxicity in standard CCK-8 cell proliferation assays (**Supplementary Fig. 27**).

The safety of the DNA nanorobots was further characterized in normal Bama miniature pigs, which exhibit high similarity to humans in anatomy and physiology[29]. Intravenous injections of free thrombin at 150 U/pig, a dose equivalent to the accumulated therapeutic dose of thrombin in the mouse model treated with nanorobots, had no effect on blood coagulation parameters (**Supplementary Table 3**) and did not induce thrombosis in major organs (**Supplementary Fig. 28a**–**c**). However, activated partial thromboplastin time (APTT) prolongation occurred but was still under 43 s after single or multiple injections of thrombin at up to 350 U/pig; D-dimer content also increased after injection of this dose, but disappeared with a final measurement of normal levels 3 d after the last treatment, indicating a transient and reversible blood coagulation system activation with no visible thrombotic formation in major tissues. Treatment with nanorobot-Th system did not lead to any significant variations in the blood coagulation parameters (**Supplementary Fig. 28d**,**e** and **Supplementary Table 3**) or histological morphology (**Supplementary Fig. 28f**) when compared to the control group, demonstrating that the nanorobot-Th is decidedly safe in the normal tissues of large animals. Although intra-arterial embolization, such as transhepatic arterial embolization (TAE) and transhepatic arterial chemoembolization (TACE), is routine practice for the effective treatment of a variety of hepatic malignancies, assisted by image-guided therapy[30], vascular occlusion-based cancer therapies remain challenging owing to the lack of safe and effective vessel-occluding agents that can be administered systemically.

We have developed a nanorobotic system for the intelligent delivery of therapeutic thrombin *in vivo* to tumor-associated blood vessels, to elicit highly efficient blockage of tumor blood supply and inhibition of tumor growth. The thrombin-delivery DNA nanorobot—with tumor-targeted delivery, recognition of tumor microenvironmental signals, triggered nanostructural changes and payload exposure—advances the application of DNA nanotechnology for cancer therapy. In a melanoma mouse model, the nanorobot not only affected the primary tumor, but also prevented the formation of metastasis, showing promising therapeutic potential.

DNA nanorobotic systems, such as the one we describe here with targeting and triggered release properties, may inspire the design of novel cancer therapeutics modified with different targeting ligands to mediate delivery of multiple biologically active payloads, such as short interfering RNA (siRNA), chemotherapeutics or peptide drugs. Combinations of different rationally designed nanorobots carrying various agents may help to accomplish the ultimate goal of cancer research: the eradication of solid tumors and vascularized metastases. Furthermore, the current strategy may be further developed as a drug delivery method for the treatment of other diseases by modification of the geometry of the nanostructures, the targeting groups and the loaded cargoes.

METHODS

Methods, including statements of data availability and any associated accession codes and references, are available in the online version of the paper.

Note: Any Supplementary Information and Source Data files are available in the online version of the paper.

ACKNOWLEDGMENTS

The authors thank L.Z. Xu (Medical and Health Analysis Center of Peking University) for animal imaging and G. Z. Shi (Laboratory Animal Center of Institute of Biophysics, Chinese Academy of Sciences) for histological examination of minipigs. We also thank A. Sheftel from High Impact Editing for improving the English of the manuscript. This work was supported by grants from National Basic Research Plan of China (MoST Program 2016YFA0201601 to G.N. and B.D.), the National Natural Science Foundation of China (31730032 to G.N., 21222311, 21573051, 91127021 to B.D., the National Distinguished Young Scientists program 31325010 to G.N.), Innovation Research Group of National Natural Science Foundation (11621505 to G.N. and Yuliang Z., 21721002 to B.D.), Beijing Municipal Science & Technology Commission (Z161100000116035 to G.N., Z161100000116036 to B.D.), CAS Interdisciplinary Innovation Team to B.D., G.N. & Yuliang Z., Key Research Program of Frontier Sciences, CAS, Grant No. QYZDB-SSW-SLH029 to B.D. and US National Institute of Health Director's Transformative Research Award (R01GM104960-01 to H.Y.).

AUTHOR CONTRIBUTIONS

Suping L., Q.J., Shaoli L., Yinlong Z., Y.T., C.S., B.D., Yuliang Z. and G.N. conceived and designed the experiments. Suping L., Q.J., Shaoli L., Yinlong Z., C.S., Y.T. and C.Z. performed the experiments. Y.T., C.S., H.Y., B.D., Yinlong Z. and G.N. collected and analyzed the data. J.W., G.A., J.H., Yiguo Z., Y.C., Y.L., L.C., G.-B.Z., G.Z. and C.Z. provided suggestions and technical support on the project. H.Y., B.D., Yuliang Z., and G.N. supervised the project. Suping L., Q.J., H.Y., B.D. and G.N. wrote the manuscript. All authors discussed the results and commented on the manuscript.

COMPETING FINANCIAL INTERESTS

The authors declare competing financial interests: details are available in the online version of the paper.

1. Seeman, N.C. DNA in a material world. *Nature* **421**, 427–431 (2003).
2. Modi, S., Nizak, C., Surana, S., Halder, S. & Krishnan, Y. Two DNA nanomachines map pH changes along intersecting endocytic pathways inside the same cell. *Nat. Nanotechnol.* **8**, 459–467 (2013).
3. Douglas, S.M., Bachelet, I. & Church, G.M. A logic-gated nanorobot for targeted transport of molecular payloads. *Science* **335**, 831–834 (2012).
4. Amir, Y. *et al.* Universal computing by DNA origami robots in a living animal. *Nat. Nanotechnol.* **9**, 353–357 (2014).
5. Huang, Y. *et al.* The angiogenic function of nucleolin is mediated by vascular endothelial growth factor and nonmuscle myosin. *Blood* **107**, 3564–3571 (2006).
6. Jungmann, R. *et al.* Multiplexed 3D cellular super-resolution imaging with DNA-PAINT and Exchange-PAINT. *Nat. Methods* **11**, 313–318 (2014).
7. Bhatia, D., Surana, S., Chakraborty, S., Koushika, S.P. & Krishnan, Y. A synthetic icosahedral DNA-based host-cargo complex for functional in vivo imaging. *Nat. Commun.* **2**, 339 (2011).
8. Lee, H. *et al.* Molecularly self-assembled nucleic acid nanoparticles for targeted in vivo siRNA delivery. *Nat. Nanotechnol.* **7**, 389–393 (2012).
9. Chauhan, V.P. & Jain, R.K. Strategies for advancing cancer nanomedicine. *Nat. Mater.* **12**, 958–962 (2013).
10. Huang, X. *et al.* Tumor infarction in mice by antibody-directed targeting of tissue factor to tumor vasculature. *Science* **275**, 547–550 (1997).
11. Hu, P. *et al.* Comparison of three different targeted tissue factor fusion proteins for inducing tumor vessel thrombosis. *Cancer Res.* **63**, 5046–5053 (2003).
12. Jain, R.K. Normalization of tumor vasculature: an emerging concept in antiangiogenic therapy. *Science* **307**, 58–62 (2005).
13. Agemy, L. *et al.* Nanoparticle-induced vascular blockade in human prostate cancer. *Blood* **116**, 2847–2856 (2010).
14. Sambrano, G.R., Weiss, E.J., Zheng, Y.W., Huang, W. & Coughlin, S.R. Role of thrombin signalling in platelets in haemostasis and thrombosis. *Nature* **413**, 74–78 (2001).
15. Pinheiro, A.V., Han, D., Shih, W.M. & Yan, H. Challenges and opportunities for structural DNA nanotechnology. *Nat. Nanotechnol.* **6**, 763–772 (2011).
16. Rothemund, P.W.K. Folding DNA to create nanoscale shapes and patterns. *Nature* **440**, 297–302 (2006).
17. Gerling, T., Wagenbauer, K.F., Neuner, A.M. & Dietz, H. Dynamic DNA devices and assemblies formed by shape-complementary, non-base pairing 3D components. *Science* **347**, 1446–1452 (2015).
18. Benson, E. *et al.* DNA rendering of polyhedral meshes at the nanoscale. *Nature* **523**, 441–444 (2015).
19. Schüller, V.J. *et al.* Cellular immunostimulation by CpG-sequence-coated DNA origami structures. *ACS Nano* **5**, 9696–9702 (2011).
20. Jiang, Q. *et al.* DNA origami as a carrier for circumvention of drug resistance. *J. Am. Chem. Soc.* **134**, 13396–13403 (2012).
21. Zhang, Q. *et al.* DNA origami as an in vivo drug delivery vehicle for cancer therapy. *ACS Nano* **8**, 6633–6643 (2014).
22. Chen, Y.J., Groves, B., Muscat, R.A. & Seelig, G. DNA nanotechnology from the test tube to the cell. *Nat. Nanotechnol.* **10**, 748–760 (2015).
23. Soundararajan, S., Chen, W., Spicer, E.K., Courtenay-Luck, N. & Fernandes, D.J. The nucleolin targeting aptamer AS1411 destabilizes Bcl-2 messenger RNA in human breast cancer cells. *Cancer Res.* **68**, 2358–2365 (2008).
24. Nutiu, R. & Li, Y. Structure-switching signaling aptamers. *J. Am. Chem. Soc.* **125**, 4771–4778 (2003).
25. Blanco, E., Shen, H. & Ferrari, M. Principles of nanoparticle design for overcoming biological barriers to drug delivery. *Nat. Biotechnol.* **33**, 941–951 (2015).
26. Kong, G., Braun, R.D. & Dewhirst, M.W. Hyperthermia enables tumor-specific nanoparticle delivery: effect of particle size. *Cancer Res.* **60**, 4440–4445 (2000).
27. Zhang, H. *et al.* Identification of urine protein biomarkers with the potential for early detection of lung cancer. *Sci. Rep.* **5**, 11805 (2015).
28. Surana, S., Shenoy, A.R. & Krishnan, Y. Designing DNA nanodevices for compatibility with the immune system of higher organisms. *Nat. Nanotechnol.* **10**, 741–747 (2015).
29. Liu, Y., Zeng, B.H., Shang, H.T., Cen, Y.Y. & Wei, H. Bama miniature pigs (Sus scrofa domestica) as a model for drug evaluation for humans: comparison of in vitro metabolism and in vivo pharmacokinetics of lovastatin. *Comp. Med.* **58**, 580–587 (2008).
30. Goldberg, S.N. *et al.* Image-guided tumor ablation: proposal for standardization of terms and reporting criteria. *Radiology* **228**, 335–345 (2003).

ONLINE METHODS

Materials and reagents. Oligonucleotides (origami staple strands and functional strands) were purchased from Invitrogen (Shanghai, China) and used without further purification. The dye-labeled DNA strands were further purified for use by denaturing PAGE (PAGE). For flow cytometry and immunohistochemistry, the following antibodies[31,32] were used for nucleolin (Sigma-Aldrich, St. Louis, MO, catalog no. N2662); mouse platelet CD41 (BD Pharmingen, San Diego, CA, catalog No. 553847); P-selectin (BD Pharmingen, San Diego, CA, catalog No. 553744); CD34 (Sigma-Aldrich, St. Louis, MO, catalog No. WH0000947M1); FITC-conjugated goat anti-rabbit IgG (BD Pharmingen, San Diego, CA, catalog No. 554020); FITC-conjugated goat anti-mouse IgG (BD Pharmingen, San Diego, CA, catalog No. 5540001) and Alexa Fluor 488 AffiniPure Donkey anti-rat IgG (Yeasen Biotech, Shanghai, China, catalog No. 34406ES60). Cell culture media, FBS, hemocytometer, and cell culture supplies were purchased from Fisher Scientific. Tris-base, acetic acid, sodium chloride, EDTA disodium salt dehydrate and other common chemical reagents were purchased from Sigma-Aldrich.

DNA origami design details. Production of M13 bacteriophage single-stranded DNA was according to Douglas *et al.*'s methods[33]. In detail, JM109 *Escherichia coli* were cultured overnight in LB medium, 5 ml were diluted in 2 × YT medium with 5 mM $MgCl_2$ and placed in a 37 °C shaker. When the optical density (OD 600) reached 0.5, p7249 M13 phages were mixed with the bacteria, and the culture incubated in a 37 °C shaker. After a 5 h incubation, the culture was collected and centrifuged at 6,000*g* for 30 min to remove the bacteria pellets. NaCl (30 g/l) and PEG (40 g/l) were added to the supernatant containing phages and the mixture was incubated on ice for 1 h. After 30 min centrifugation at 10,000*g*, the phage pellet was collected and suspended in Tris-Cl (10 mM, pH 8.5). After adding 0.2 M NaOH and 1% SDS, the phage solution was mixed and incubated at 25 °C for 3 min. After the addition of potassium acetate (3 M, pH5.5) for neutralization, the solution was incubated on ice for 10 min and centrifuged (12,000*g*, 30 min). The ssDNA (7249 nt)-containing supernatant was collected and precipitated in ethanol (70%) on ice for 2 h. After centrifuging at 12,000*g* for 30 min, the DNA pellet was collected and washed in ethanol (70%) and then resuspended in Tris-Cl (10 mM, pH 8.5). The concentrations of ssDNA were determined by UV-Vis spectrometry (Shimadzu Corp. Kyoto, Japan).

The original design of the rectangular DNA origami structure shown in **Supplementary Figure 1** was established by Rothemund[16]. This design was used as the blank template in this work and functional strands were used to replace the original strands at the corresponding positions. The position and sequences of the functional staple strands are shown in different colors in **Supplementary Figures 1–3** and **Supplementary Note 1**.

Rectangular DNA nanosheets. Rectangular DNA nanostructures were made by mixing a long single-stranded scaffold strand (7249 DNA derived from M13 bacteriophage) with short strands (including staple strands and functional strands) in 1 × TAE-Mg buffer (40 mM Tris, 20 mM acetic acid, pH 8.0, 2 mM EDTA, 12.5 mM $Mg(CH_3COOH)_2$). The final concentrations of scaffold DNA and basic staple strands were 10 nM and 80 nM, respectively. The mixture was heated to 65 °C, then annealed by cooling to 25 °C at a rate of 10 min/°C using an Eppendorf thermal cycler (Eppendorf Mastercycler ep Gradient S, Hamburg, Germany). Unless otherwise stated, all DNA strands or aptamers were purchased from the oligonucleotide synthesis service of Invitrogen (Invitrogen, Carlsbad, CA).

The resulting rectangular DNA origami sheets were separated from excess staple strands using Amicon Ultra-0.5 ml 100 kD centrifugal filters (Millipore Corporation, Bedford, USA). The initial filtration was performed by adding 350 µl 1 × TAE-Mg buffer to 100 µl DNA sheets, and centrifuging for 3 min at 2,075*g*. Then two wash steps were performed by adding 350 µl 1 × TAE-Mg buffer and centrifuging for 3 min each at 2,075*g*. The remaining solution was collected and characterized using 1% agarose gel electrophoresis and atomic force microscopy (AFM).

Preparation of thrombin–DNA conjugates and **thrombin activity analysis.** Thrombin–DNA conjugates were prepared using sulfosuccinimidyl-4-(*N*-maleimidomethyl) cyclohexane-1-carboxylate (sulfo-SMCC, Sigma-Aldrich, St. Louis, MO) as a bifunctional cross-linker between thrombin and DNA. In a typical synthesis, 200 µl 3 µM thrombin (Sigma-Aldrich, St. Louis, MO, catalog No. T4648) was mixed with 9 µl 15 mM sulfo-SMCC at room temperature for 1 h. Excess sulfo-SMCC was removed using an Amicon Ultra-0.5 ml 30 kD centrifugal filter and washing three times by centrifugation. The initial washing was conducted by adding 250 µl PBS to 200 µl of the mixture of sulfo-SMCC and thrombin, and centrifuging for 3 min at 5,534*g*. The subsequent two washing steps were performed by adding 350 µl PBS and centrifuging for 3 min at 5,534*g*. The residual solution was collected and a 15-fold excess of thiolated poly-T DNA was added. The mixture was incubated at 4 °C overnight and the final thrombin–DNA conjugates were purified using 30 kD centrifugal filters. Conjugation was verified by 4–12% SDS-PAGE.

Thrombin activity was assayed using tosyl-glycyl-prolyl-arginine-4-nitroanilide acetate (chromozym TH) as a substrate, following the manufacturer's protocol (Boehringer Mannheim, Indianapolis, IN). In brief, reactions were conducted at 37 °C for 5 min, 10 min, 30 min, 1 h or 1.5 h, with free thrombin as a positive control and a blank DNA sheet as a negative control. Thrombin–DNA conjugates and DNA sheets loaded with thrombin were assayed at concentrations equivalent to 90 nM thrombin and at a substrate concentration of 2 mg/ml. Reactions were carried out in a volume of 100 µl. The increase in absorbance at 405 nm was monitored on a Beckman DU-30 spectrophotometer.

Thrombin-loaded tubular-DNA nanorobot. Thrombin–DNA conjugates were mixed with the rectangular DNA origami structures (containing thrombin capture strands) at a molar ratio of 10:1 in 1 × TAE-Mg buffer. The mixture was heated to 45 °C, then cooled to 25 °C at a rate of 10 min/°C to facilitate annealing. The thrombin-rectangle-origami assemblies were purified using 100 kD centrifugal filters to remove excess thrombin–DNA conjugates. Tube origami structures were then constructed by adding a 20-fold molar excess of fasteners to the thrombin-rectangle-origami, and then a fivefold molar excess of additional targeting strands was added to the mixture. To facilitate assembly, the mixture was heated to 37 °C, then cooled to 15 °C at a rate of 10 min/°C.

Platelet aggregation. Fresh blood from healthy volunteers (informed consent was obtained from all subjects) was collected using ACD (2.5% trisodium citrate, 2.0% D-glucose, 1.5% citric acid) as the anticoagulant. Platelets were washed with CGS buffer (0.123 M NaCl, 0.033 M D-glucose and 0.013 M trisodium citrate, pH 6.5), and resuspended in modified Tyrode's buffer (2.5 mM Hepes, 150 mM NaCl, 2.5 mM KCl, 12 mM $NaHCO_3$, 5.5 mM D-glucose, pH 7.4), supplemented with 1 mM $CaCl_2$ and 1 mM $MgCl_2$, to a final concentration of 3×10^8/ml. After incubation at 22 °C for 2 h, platelet aggregation was assessed using a turbidometric platelet aggregometer (Xinpusen, Chengdu, China) by adding 0.3 ml of washed platelets and free thrombin, DNA origami sheets, DNA-origami sheets with conjugated thrombin or DNA-origami tubes with conjugated thrombin (at equivalent thrombin concentrations where appropriate) into glass aggregometer cuvettes at 37 °C under stirring.

DNA nanorobot preparation for *in vitro* and *in vivo* imaging. Thrombin-loaded rectangular DNA nanostructures with imaging strands were mixed with fluorescent-dye-conjugated DNA in 1 × TAE-Mg buffer. The molar ratio of dye-modified DNA to each imaging strand was 3:1. The mixtures were heated to 45 °C, then cooled to 25 °C at a steady rate of 10 min/°C using an Eppendorf Mastercycler. Excess dye-modified DNA was removed using 100 kD centrifugal filters. A 20-fold molar excess of fasteners and a fivefold molar excess of targeting strands, including the AS1411 sequence, were subsequently added. The mixture was heated to 37 °C, then cooled to 15 °C at a rate of 10 min/°C to promote assembly.

Cell culture. All cell lines were purchased from the American Type Culture Collection (Manassas, VA, USA) unless stated otherwise. The human breast cancer cell line MDA-MB-231, and human umbilical vein endothelial cells (HUVECs) were maintained in DMEM supplemented with 10% FBS, 100 U/ml penicillin and 100 U/ml streptomycin. The human ovarian cancer cell line SK-OV3 (Shanghai Institutes for Biological Sciences, Shanghai, China) was maintained in McCoy's 5A medium supplemented with 10% FBS, 100 U/ml

penicillin and 100 U/ml streptomycin. The murine melanoma cell line B16-F10 was grown in RPMI 1640 medium supplemented with 10% FBS, 1% penicillin and streptomycin. Mouse brain endothelial cells (bEnd.3) were maintained in high-glucose DMEM supplemented with 10% FBS, 100 U/ml penicillin and 100 U/ml streptomycin. Cell line authentication was performed by short tandem repeat DNA profiling and comparison with a reference database. The cells were cultured at 37 °C, 5% CO_2 and were routinely tested for mycoplasma contamination.

Cell surface expression of nucleolin. The expression of nucleolin on the cell surface was assessed with antibodies specific to human nucleolin using a Beckman Coulter CyAn ADP flow cytometer (Fullerton, CA, USA). HUVECs were trypsinized, washed twice in PBS, resuspended in 10% goat serum in PBS, and incubated at 4 °C for 30 min. Cells were then pelleted and resuspended in 2% goat serum in PBS containing 20 μg/ml anti-nucleolin antibody. After 1 h incubation on ice, cells were washed three times with PBS and incubated with a 1:500 dilution of FITC-conjugated goat anti-rabbit IgG in PBS for 30 min on ice. Cells were washed with PBS twice and analyzed by flow cytometry.

Cell surface binding of AS1411 aptamer-containing DNA strands. HUVECs were prepared and blocked with goat serum. FITC-labeled F50-containing the AS1411 aptamer sequence (5′- FITC-**GGTGGTGGTGGTTGTGGTGG TGGTGG** TCTAAAGTTTTGTCGTGAATTGCG -3′, the region of AS1411 aptamer is in bold font) that can recognize nucleolin on the surface of HUVECs was used. Cells were incubated with 2 μM FITC-labeled F50 strands (Invitrogen, Carlsbad, CA) or 2 μM random DNA sequence (5′-GAGAACCT GAGTCAGTATTGCGGAGATCTAAAGTTTTGTCGTGAATTGCG -3′) as a control for 2 h at 37 °C. Cells were washed twice with PBS and assayed by flow cytometry using a BD Biosciences BD Accuri C6 flow cytometer (San Jose, CA, USA).

Aptamer competition assays. To determine whether cell surface binding of the F50 DNA strand was specific for nucleolin, HUVECs were pretreated with antibodies against human nucleolin at 45 μg/ml before addition of the aptamer. Cells were then incubated with 2 μM FITC-labeled F50 for 2 h at 37 °C. Next, the cells were washed with PBS twice as described above and analyzed by flow cytometry.

Binding of F50 and fastener strands. HUVECs were prepared and treated with goat serum. Cells were then incubated with 2 μM FITC-labeled F50, which are Y-shaped DNA structures with either a 15 base pair duplex (F50 + C15) or a 26 base pair duplex (F50 + C26) that was annealed in 1× TAE/Mg buffer, for different durations. Cells were washed with PBS twice as detailed above and analyzed by flow cytometry.

The DNA sequences used are shown below:

F50 + C15, mixture of fastener:

5′-FITC-GGTGGTGGTGGTTGTGGTGGTGGTGGTCTAAAGTTTTG TCGTGAATTGCG-3′ and 5′-GTAAAGCTTTTTTTTTTTTACAACCAC CACCACC -3′;

F50 + C26, mixture of fully complementary AS1411 portion structures:

5′ end FITC-labeled F50 and 5′-GTAAAGCACCACCACCACCACAAC CACCACCACC -3′.

Fastener duplex opening by recombinant nucleolin. 20 μM mixtures of the Y-shaped structures in 1× TAE/Mg buffer were heated to 95 °C and then annealed by cooling to 25 °C at a rate of 3 min/°C using an Eppendorf thermal cycler. The DNA sequences used are shown below:

F50 + C15, mixture of fastener:

5′-FITC-GGTGGTGGTGGTTGTGGTGGTGGTGGTCTAAAGTTTTGT CGTGAATTGCG-3′ and

5′-GTAAAGCTTTTTTTTTTTTACAACCACCACCACC –BHQ1-3′;

F50 + C26, mixture of fully complementary AS1411 portion structures:

5′-FITC-GGTGGTGGTGGTTGTGGTGGTGGTGGTCTAAAGTTTTG TCGTGAATTGCG-3′ and 5′-GTAAAGCACCACCACCACCACAACCAC CACCACC–BHQ1-3′.

A tenfold molar excess of recombinant nucleolin (RPC242Hu01, Cloud-Clone Corp.) was added and incubated with the Y-shaped DNA structures (F50 + C15 and F50 + C26, 2 μM) at 37 °C. Fluorescence intensity measurements were performed with a fluorescence spectrometer (LS55, Perkin Elmer).

Fastener duplex opening by cell-surface-expressed nucleolin. The 20 μM mixtures of Y-shaped structures in 1× TAE/Mg buffer were heated to 95 °C and then annealed by cooling to 25 °C at a rate of 3 min/°C using an Eppendorf thermal cycler.

The DNA sequences used are shown below:

F50 + C15, mixture of fastener:

5′-FITC-GGTGGTGGTGGTTGTGGTGGTGGTGGTCTAAAGTTTTG TCGTGAATTGCG-3′

and 5′-GTAAAGCTTTTTTTTTTTTACAACCACCACCACC –BHQ1-3′;

F50 + C26, mixture of fully complementary AS1411 portion structures:

5′-FITC-GGTGGTGGTGGTTGTGGTGGTGGTGGTCTAAAGTTTTG TCGTGAATTGCG-3′

and 5′-GTAAAGCACCACCACCACCACAACCACCACCACC–BHQ1-3′

FC + CC, mixture of no AS1411 structures:

5′-FITC-AAAAAAAAAAAAAAAAAAAAAAAAAAACTAAAGTTTTG TCGTGAATTGCG-3′and 5′-GTAAAGCTTTTTTTTTTTTTTTTTTTT TTTTTT-BHQ1-3′.

HUVECs were prepared and blocked with goat serum as detailed above. Cells were then incubated with the Y-shaped DNA structures (F50 + C15, F50 + C26 and FC + CC) at a concentration of 2 μM for 2 h at 37 °C. Cells were washed twice with PBS and assayed using flow cytometry.

DNA nanorobot opening by recombinant nucleolin. We designed six pairs of fasteners consisting of 5′-FITC-labeled F50 and 3′-BHQ1-labeled Comp15: FITC-F50-48, Comp15-48-Q; FITC-F50-73, Comp15-73-Q; FITC-F50-97, Comp15-97-Q; FITC-F50-120, Comp15-120-Q; FITC-F50-144, Comp15-144-Q; and FITC-F50-169, Comp15-169-Q. The fluorophore–quencher pairs served as switchable fluorescent beacons. 20 μM mixtures of fluorophore–quencher pairs in 1× TAE/Mg buffer were heated to 95 °C and then annealed by cooling to 25 °C at a rate of 3 min/°C using an Eppendorf thermal cycler. A 20-fold molar excess of fluorophore–quencher fasteners was added to the DNA sheets. The mixture was heated to 37 °C, then cooled to 15 °C at a rate of 10 min/°C to promote assembly. Extra fastened pairs were removed using filtration devices.

The DNA sequences used are shown below:

FITC-F50-48:

5′-FITC-GGTGGTGGTGGTTGTGGTGGTGGTGGTCTAAAGTTTTG TCGTGAATTGCG-3′

Comp15-48-Q:

5′-GTAAAGCTTTTTTTTTTTTACAACCACCACCACC-BHQ1-3′

FITC-F50-73

5′-FITC-GGTGGTGGTGGTTGTGGTGGTGGTGGTAGAGCTTGACG GGGAAATCAAAA-3′

Comp15-73-Q

5′-TGTAGCATTTTTTTTTTTTACAACCACCACCACC-BHQ1-3′

FITC-F50-97

5′-FITC-GGTGGTGGTGGTTGTGGTGGTGGTGGCGAGAAAGGAAG GGAACAAACTAT-3′

Comp15-97-Q

5′-TGAGTTTCTTTTTTTTTTTACAACCACCACCACC-BHQ1-3′

FITC-F50-120

5′-FITC-GGTGGTGGTGGTTGTGGTGGTGGTGGATAGGAACCCAT GTACAAACAGTT-3′

Comp15-120-Q

5′-CAAGCCCATTTTTTTTTTTTACAACCACCACCACC-BHQ1-3′

FITC-F50-144

5′-FITC-GGTGGTGGTGGTTGTGGTGGTGGTGGCACCACCCTCAT TTTCCTATTATT-3′

Comp15-144-Q

5′-CCGCCAGCTTTTTTTTTTTTACAACCACCACCACC-BHQ1'-3′

FITC-F50-169

5′FITC-GGTGGTGGTGGTTGTGGTGGTGGTGGCTACATTTTGACG CTCACCTGAAA-3′

Comp15-169-Q

doi:10.1038/nbt.4071

5′-CCCTCAGTTTTTTTTTTTTACAACCACCACCACC-BHQ1-3′.

A 20-fold molar excess of recombinant nucleolin was added and incubated with DNA nanorobots labeled by fluorophore–quencher fasteners at 37 °C. Fluorescence intensity measurements were performed with a fluorescence spectrometer (LS55, Perkin Elmer).

Cell surface nucleolin triggering of DNA nanorobot reconfiguration. 20 μM mixtures of FRET pairs in 1× TAE/Mg buffer were heated to 95 °C and then annealed by cooling to 25 °C at a rate of 3 min/°C using an Eppendorf thermal cycler. A 20-fold molar excess of FRET fasteners was added to the DNA sheets. The mixture was heated to 37 °C, then cooled to 15 °C at a rate of 10 min/°C to promote assembly.

HUVECs were prepared and blocked with goat serum as described above. Serum-starved HUVECs where surface nucleolin expression was downregulated were also used. Non-starved and serum-starved cells were incubated with DNA nanorobots labeled with fluorophore–quencher fasteners for 2 h at 37 °C. Cells were washed twice with PBS and assayed using flow cytometry.

Cell binding of nanorobot. HUVECs were trypsinized, washed twice with 1 ml PBS, seeded onto Lab-Tek Chamber Slides (Nunc) and cultured overnight. Cells were then incubated with either 15 μM Alexa 594-labeled AS1411 aptamer or Alexa 594-labeled nanorobots or nanotubes at a concentration equivalent to 15 μM F50 at 37 °C for different time periods. To determine whether binding of the nanorobot was dependent on surface nucleolin, the cells were pretreated with anti-nucleolin antibodies (45 μg/ml). After treatment, the cells were washed three times with PBS and fixed with 4% paraformaldehyde for 30 min. Then the cells were stained with DIO (plasma membrane) and DAPI (nucleus) (Sigma-Aldrich, St. Louis, MO) and imaged with a Nikon Ti-e microscope equipped with an UltraVIEW Vox confocal attachment (Perkin Elmer, Boston, MA, USA).

Animal studies. All animal studies were performed in accordance with ARRIVE guidelines, with the approval of the Ethics of Animal Experiments of the Health Science Center of Peking University Committee. Six to eight-week-old female nude mice (nu/nu) and C57BL/6J mice were obtained from Vital River Laboratory Animal Technology Co. Ltd. (Beijing, China) and housed with a 12 h light/dark cycle at 22 °C and food and water *ad libitum*. For the Kras mutant lung cancer mouse model, we used doxycycline-inducible Kras mutant mice. The doxycycline-inducible Kras model was generated using transgenic *TetO-Kras^{G12D}* mice as reported[27]. A pCYL50 construct harboring *TRE-Kras^{G12D}* expression elements was used to generate single-copy integrated transgenic mice through the "sleeping-beauty" system. When the founder was crossed with CC10rtTA, and the bitransgenic progeny were fed with a doxycycline diet at 6 weeks old, expression of *Kras^{G12D}* transgene was efficiently induced. Bama miniature pigs (*Sus scrofa domestica*) weighing 20 to 25 kg (8–10 months old, half male and half female) were also used in the study. All pigs were healthy and maintained in the animal facility at the Farm Animal Research Center (Beijing, China) under standard conditions prescribed by the Institutional Guidelines. The study protocol was approved by the Institutional Animal Care and Use Committee of the Institute of Zoology, Chinese Academy of Sciences.

***In vivo* targeting.** MDA-MB-231 cells (2.0×10^6) mixed with an equal volume of Matrigel (BD Pharmingen, San Diego, CA), were injected subcutaneously into the mammary fat pads of female nude mice. When the tumor size reached ~100 mm^3, as determined using digital calipers, the mice received tail-vein injections of Cy5.5-labeled DNA nanorobot and were examined using an *in vivo* optical imaging system (Maestro, CRi Inc., Woburn, MA, USA) at various time points thereafter. For biodistribution analysis, the mice were euthanized at the indicated time points post-injection and the tumors and major organs were harvested.

Staining of tissues. For histological examination, tumors and major organs were collected from MDA-MB-231-bearing nude mice at the indicated time points post-administration of DNA nanorobot-Th and various controls. Tissue samples were fixed in 4% paraformaldehyde, immunostained with anti-CD41 antibody for thrombosis or anti-CD34 antibody for endothelial cells. For evaluating tissue necrosis, sections were stained with hematoxylin and eosin (H&E).

***In vivo* therapeutic efficacy.** To assess the *in vivo* efficacy of the nanorobots, nude mice bearing ~100 mm^3 MDA-MB-231 tumors were randomly divided into six groups of eight mice per treatment group and treated with saline, free thrombin, empty nanorobot, nontargeted nanotube-Th, targeted nanotube-Th or nanorobot-Th (~1.5 U accumulated thrombin / mouse), by tail vein injection every 3 d for a total of six treatments. The day of the first injection was designated day 0. Tumors were measured with calipers in three dimensions. The following formula was used to calculate tumor volume: Volume = length × width^2/2.

To confirm antitumor efficacy, a syngeneic B16-F10 melanoma tumor model was established by subcutaneous injection of 5×10^6 murine B16-F10 cells into the right posterior flank of C57BL/6J mice. When the tumors reached a size of ~150 mm^3, the mice (ten mice per group) were treated intravenously with saline, free thrombin, empty nanorobot, nontargeted nanotube-Th, targeted nanotube-Th or nanorobot-Th every other day for 14 d. Tumor volume was determined as described above. The animals were euthanized 2 d after the last treatment, and the livers were excised and weighed. Liver sections were stained with H&E for metastasis analysis.

Two other tumor models, an ovarian cancer SK-OV3 xenograft model and an inducible Kras^{G12D} lung tumor model were used to investigate the versatility of nanorobot-Th. For the SK-OV3 model, nude mice bearing ~100 mm^3 SK-OV3 xenografts (eight mice per group) were treated intravenously with saline, free thrombin, empty nanorobot, a scrambled aptamer control, nontargeted nanotube-Th, targeted nanotube-Th or nanorobot-Th every 3 d for a total of 6 treatments (~1.5 U accumulated thrombin/mouse).

The inducible Kras^{G12D} mice were fed with doxycycline diet since the 6th week after birth to induce primary lung adenomas. After being induced for 2 weeks, mice with tumors were randomly divided into four groups (three animals per group) and treated with saline, free thrombin, nontargeted nanotube-Th or nanorobot-Th, respectively, by intravenous injection once every 3 d. The progress of lung tumors was monitored by MR imaging 1 week and 2 weeks after treatment started.

***In vivo* MR imaging.** *TetO-Kras^{G12D}* transgenic mice were imaged using a 7.0 T Bruker Biospec animal MRI instrument (Germany). The imaging parameters were set as follows: FOV (field of view) = 3 × 3 cm^2, MTX (matrix size) = 256 × 256, slice thickness = 1 mm, TE = 61.2 ms, TR = 2320 ms, and NEX = 4. The mice were anesthetized with 1.5% isoflurane delivered via nose cone before and during the imaging sessions.

Cell viability assay. The cytotoxicity of DNA nanorobot was assessed in murine endothelial bEnd3 cells. Cells (2,000 cells/well) were added to the wells of a 96-well plate (Corning, Woburn, MA, USA). After culturing at 37 °C for 4 h, the cells were incubated with DNA nanorobot-Th at either 3.3 nM or 6.6 nM (in PBS) for a further 24, 48 or 72 h. The proportion of viable cells was evaluated using a CCK-8 kit (Sigma-Aldrich, St. Louis, MO, catalog No. 96992). Blank wells only with culture media and PBS-treated wells were used to define 0 and 100% viability, respectively.

Determination of platelet surface P-selectin, plasma fibrin and thrombin levels and platelet counts. Nude mice bearing MDA-MB-231 tumors were injected intravenously with DNA nanorobot-Th every 2 d for a total of six injections. Mouse whole blood was then collected retro-orbitally into a 3.8% sodium citrate solution in blood collection tubes at the indicated time points. For platelet activity studies, the blood was mixed with an equal volume of 2% paraformaldehyde for 30 min at RT and centrifuged to obtain platelet-rich plasma (PRP). The PRP was incubated with FITC-conjugated P-selectin-specific monoclonal antibodies and analyzed by flow cytometry. Fibrin or thrombin levels in the PRP were quantified by enzyme-linked immunosorbent assay (ELISA) kits (Abcam, ab108844 and ab157527, respectively). Platelet numbers were counted manually with a hemocytometer using optical microscopy.

ELISA for serum cytokines. Non-tumor-bearing C57BL/6J mice were injected intravenously with DNA nanorobot-Th every 2 d for a total of six

injections (n = 3 mice). Mouse serum was obtained by centrifuging whole blood taken by retro-orbital venous puncture at different time points. Serum cytokine concentrations including IL-6, IP-10, TNFα (R&D Systems, China, Shanghai, China, SM6000B, SMCX100, SMTA00B) and IFNα (ThermoFisher Scientific, Shanghai, China, KMC4011) were measured by ELISA as per the manufacturer's protocol using 50 μl serum[34–37].

***In vivo* thrombotic risk assessment in Bama miniature pigs.** To evaluate the *in vivo* safety of DNA nanorobot-Th, Bama minipigs were randomly divided into three groups of three pigs per treatment group as follows: group 1, saline; group 2, free thrombin at a dose of 150 U thrombin/pig (equivalent to ~1.5 U accumulated thrombin/mouse); group 3, nanorobot-Th. The animals were injected via marginal ear vein every other day for a total of three injections. Day 0 marks the first day of injection. Blood was collected from the marginal ear vein into sodium citrate (3.8% flnal concentration) at different time points (0 h, 2 h, 24 h, 3 d and 5 d) and immediately sent to the Clinical Laboratory, Changping hospital, Beijing, China, for measurements of coagulation parameters. At this institute, normal values for these parameters are as followings: PT: 11.5-15 s; APTT: 28-43 s; TT: 13-21 s; Fibrinogen: 2-4 g/l; D-dimer: 0-0.5 μg/ml. The animals were killed 3 d after the last treatment and the major organs were excised and stained with H&E for histological examination. The following formula was used to perform dose conversion between mice and pigs:

$$D_p = D_m \times (K_{mm} / K_{mp})$$

Where D_p is the dose injected into pigs, D_m is the dose used in mice, K_{mm} is the dose in mg/kg to dose in mg/m^2 conversion factor of mice and K_{mp} is the dose in mg/kg to dose in mg/m^2 conversion factor of the pigs.

Blinding. All experimental procedures and quantification of results, including injections, isolation of the tumors or organs, tissue histological analysis and FACS, were done by two independent researchers.

Statistical analysis. Quantitative data are presented as mean ± s.d. or mean ± s.e.m. The differences between groups were compared using student's t-test or one-way analysis of variance (ANOVA) with repeated measures followed by Tukey's HSD test. Tumor volumes were compared using a Kruskal–Wallis test followed by a Mann–Whitney test. Cumulative survival in various groups were compared using Kaplan–Meier curves followed by the Log-rank test. Two-sided p values less than 0.05 were considered statistically significant. Statistics were performed using SPSS 18.0 software.

Life Sciences Reporting Summary. Further information on experimental design is available in the **Life Sciences Reporting Summary**.

Data Availability Statement. The data that support the findings of this study are available within the paper and its supplementary information files.

31. Miniard, A.C., Middleton, L.M., Budiman, M.E., Gerber, C.A. & Driscoll, D.M. Nucleolin binds to a subset of selenoprotein mRNAs and regulates their expression. *Nucleic Acids Res.* **38**, 4807–4820 (2010).
32. Thompson, J.S. *et al.* BAFF binds to the tumor necrosis factor receptor-like molecule B cell maturation antigen and is important for maintaining the peripheral B cell population. *J. Exp. Med.* **192**, 129–135 (2000).
33. Douglas, S.M., Chou, J.J. & Shih, W.M. DNA-nanotube-induced alignment of membrane proteins for NMR structure determination. *Proc. Natl. Acad. Sci. USA* **104**, 6644–6648 (2007).
34. Alvarez-Erviti, L. *et al.* Delivery of siRNA to the mouse brain by systemic injection of targeted exosomes. *Nat. Biotechnol.* **29**, 341–345 (2011).
35. Guyer, R.A. & Macara, I.G. Loss of the polarity protein PAR3 activates STAT3 signaling via an atypical protein kinase C (aPKC)/NF-κB/interleukin-6 (IL-6) axis in mouse mammary cells. *J. Biol. Chem.* **290**, 8457–8468 (2015).
36. Gottfries, J., Melgar, S. & Michaëlsson, E. Modelling of mouse experimental colitis by global property screens: a holistic approach to assess drug effects in inflammatory bowel disease. *PLoS One* **7**, e30005 (2012).
37. O'Callaghan, P., Li, J.P., Lannfelt, L., Lindahl, U. & Zhang, X. Microglial heparan sulfate proteoglycans facilitate the cluster-of-differentiation 14 (CD14)/Toll-like receptor 4 (TLR4)-dependent inflammatory response. *J. Biol. Chem.* **290**, 14904–14914 (2015).

doi:10.1038/nbt.4071

nature research

Corresponding author(s): Guangjun Nie, Hao Yan, Baoquan Ding, Yuliang zhao

☐ Initial submission ☐ Revised version ☒ Final submission

Life Sciences Reporting Summary

Nature Research wishes to improve the reproducibility of the work that we publish. This form is intended for publication with all accepted life science papers and provides structure for consistency and transparency in reporting. Every life science submission will use this form; some list items might not apply to an individual manuscript, but all fields must be completed for clarity.

For further information on the points included in this form, see Reporting Life Sciences Research. For further information on Nature Research policies, including our data availability policy, see Authors & Referees and the Editorial Policy Checklist.

Experimental design

1. Sample size

Describe how sample size was determined.

No effect size was predetermined. All the biochemical and biological experiments were performed in three replicated or more.

2. Data exclusions

Describe any data exclusions.

No animals and/or data were excluded.

3. Replication

Describe whether the experimental findings were reliably reproduced.

We replicated certain data points of our study and found similar results did not show significant difference in terms of numbers and distributions.

4. Randomization

Describe how samples/organisms/participants were allocated into experimental groups.

The dosing groups were filled by randomly selecting from the same pool of animals for in vivo experiments.

5. Blinding

Describe whether the investigators were blinded to group allocation during data collection and/or analysis.

All experimental procedures and quantification of results, including injections, isolation of the tumors or organs, tissue histological analysis and FACS, were done by two independent researchers.

Note: all studies involving animals and/or human research participants must disclose whether blinding and randomization were used.

6. Statistical parameters

For all figures and tables that use statistical methods, confirm that the following items are present in relevant figure legends (or in the Methods section if additional space is needed).

n/a	Confirmed	
☐	☒	The exact sample size (*n*) for each experimental group/condition, given as a discrete number and unit of measurement (animals, litters, cultures, etc.)
☐	☒	A description of how samples were collected, noting whether measurements were taken from distinct samples or whether the same sample was measured repeatedly
☐	☒	A statement indicating how many times each experiment was replicated
☐	☒	The statistical test(s) used and whether they are one- or two-sided (note: only common tests should be described solely by name; more complex techniques should be described in the Methods section)
☐	☒	A description of any assumptions or corrections, such as an adjustment for multiple comparisons
☐	☒	The test results (e.g. *P* values) given as exact values whenever possible and with confidence intervals noted
☐	☒	A clear description of statistics including central tendency (e.g. median, mean) and variation (e.g. standard deviation, interquartile range)
☐	☒	Clearly defined error bars

See the web collection on statistics for biologists for further resources and guidance.

Nature Biotechnology: doi:10.1038/nbt.4071

Software

Policy information about availability of computer code

7. Software

Describe the software used to analyze the data in this study.	OriginPro 8.5.1, GraphPad Prism 5, SPSS 18.0 and ImageJ 1.43u

For manuscripts utilizing custom algorithms or software that are central to the paper but not yet described in the published literature, software must be made available to editors and reviewers upon request. We strongly encourage code deposition in a community repository (e.g. GitHub). *Nature Methods* guidance for providing algorithms and software for publication provides further information on this topic.

Materials and reagents

Policy information about availability of materials

8. Materials availability

Indicate whether there are restrictions on availability of unique materials or if these materials are only available for distribution by a for-profit company.	There are no restrictions on availability of the materials used in the study.

9. Antibodies

Describe the antibodies used and how they were validated for use in the system under study (i.e. assay and species).	The following antibodies were used for nucleolin (Sigma-Aldrich, St. Louis, MO, catalog No. N2662); mouse platelet CD41 (BD Pharmingen, San Diego, CA, catalog No. 553847); P-selectin (BD Pharmingen, San Diego, CA, catalog No. 553744); CD34 (Sigma-Aldrich, St. Louis, MO, catalog No. WH0000947M1); FITC-conjugated goat anti-rabbit IgG (BD Pharmingen, San Diego, CA, catalog No. 554020); FITC-conjugated goat anti-mouse IgG (BD Pharmingen, San Diego, CA, catalog No. 5540001) and Alexa Fluor 488 AffiniPure Donkey anti-rat IgG (Yeasen Biotech, Shanghai, China, catalog No. 34406ES60). All the antibodies are validated by the manufacturers.

10. Eukaryotic cell lines

a. State the source of each eukaryotic cell line used.	All cell lines were purchased from the American Type Culture Collection (Manassas, VA, USA). The human ovarian cancer cell line SK-OV3 was obtained from Shanghai Institutes for Biological Sciences, Shanghai, China.
b. Describe the method of cell line authentication used.	Cell lines authentication was performed by short tandem repeat DNA profiling and comparison with reference database.
c. Report whether the cell lines were tested for mycoplasma contamination.	Reported in Online Methods/Cell Culture The cell lines have been tested for mycoplasma contamination routinely.
d. If any of the cell lines used are listed in the database of commonly misidentified cell lines maintained by ICLAC, provide a scientific rationale for their use.	No. HUVECs, MDA-MB-231, B16-F10, SK-OV3 and bEnd3 cell lines are not listed in the database.

Nature Biotechnology: doi:10.1038/nbt.4071

Animals and human research participants

Policy information about studies involving animals; when reporting animal research, follow the ARRIVE guidelines

11. Description of research animals

Provide details on animals and/or animal-derived materials used in the study.

All animal studies were performed in accordance with ARRIVE guidelines, with the approval of the Ethics of Animal Experiments of the Health Science Center of Peking University Committee. Six to eight-week-old female nude mice (nu/nu) and C57BL/6J mice were obtained from Vital River Laboratory Animal Technology Co. Ltd (Beijing, China) and housed with a 12 h light/dark cycle at 22°C and food and water ad libitum. For the Kras mutant lung cancer mouse model, we used doxycycline-inducible Kras mutant mice. The doxycycline-inducible Kras model was generated using transgenic TetO-KrasG12D mice as reported. A pCYL50 construct harboring TRE-KrasG12D expression elements was used to generate single-copy integrated transgenic mice through the “sleeping-beauty” system. When the founder was crossed with CC10rtTA, and the bitransgenic progeny were fed with a doxycycline diet at 6 weeks old, expression of KrasG12D transgene was efficiently induced. Bama miniature pigs (Sus scrofa domestica) weighing 20 to 25 kg (8-10 months old, half male and half female) were also used in the study. All pigs were healthy and maintained in the animal facility at the Farm Animal Research Center (Beijing, China) under standard conditions prescribed by the Institutional Guidelines. The study protocol was approved by the Institutional Animal Care and Use Committee of the Institute of Zoology, Chinese Academy of Sciences.

Policy information about studies involving human research participants

12. Description of human research participants

Describe the covariate-relevant population characteristics of the human research participants.

Fresh blood was from healthy volunteers, whose informed consent was obtained

Nature Biotechnology: doi:10.1038/nbt.4071

nature research

Corresponding author(s): Guangjun Nie, Hao Yan, Baoquan Ding, Yuliang Zhao

☐ Initial submission ☐ Revised version ☒ Final submission

Flow Cytometry Reporting Summary

Form fields will expand as needed. Please do not leave fields blank.

Data presentation

For all flow cytometry data, confirm that:

☒ 1. The axis labels state the marker and fluorochrome used (e.g. CD4-FITC).

☐ 2. The axis scales are clearly visible. Include numbers along axes only for bottom left plot of group (a 'group' is an analysis of identical markers).

☐ 3. All plots are contour plots with outliers or pseudocolor plots.

☒ 4. A numerical value for number of cells or percentage (with statistics) is provided.

Methodological details

5. Describe the sample preparation.	Online Methods/Cell surface expression of nucleolin (page 25)/Cell surface binding of AS1411 aptamer-containing DNA strands (page 25-26)/Aptamer competition assays (page 26)/Binding of F50 and fastener strands (page 26)/Fastener duplex opening by cell surface-expressed nucleolin (page 27)/Cell surface nucleolin triggering of DNA nanorobot reconfiguration (page 29)/Determination of platelet surface P-selectin, plasma fibrin and thrombin levels and platelet counts (page 32-33).
6. Identify the instrument used for data collection.	Online Methods/Cell surface expression of nucleolin (page 25)/Cell surface binding of AS1411 aptamer-containing DNA strands (page 25-26).
7. Describe the software used to collect and analyze the flow cytometry data.	FlowJo 8 software (TreeStar); ModFitLT V4.1
8. Describe the abundance of the relevant cell populations within post-sort fractions.	10000 cells were analyzed for fluorescent intensity in the defined gate.
9. Describe the gating strategy used.	A gate is drawn around the cells. Single cells are determined with the area and the height of the forward scatter (FSC). The analysis was carried out in this gate.

Tick this box to confirm that a figure exemplifying the gating strategy is provided in the Supplementary Information. ☐

Nature Biotechnology: doi:10.1038/nbt.4071

nature research

Corresponding author(s): Guangjun Nie, Hao Yan, Baoquan Ding, Yuliang zhao

☐ Initial submission ☐ Revised version ☒ Final submission

MRI Studies Reporting Summary

Form fields will expand as needed. Please do not leave fields blank.

Experimental design

1. Describe the experimental design.	Magnetic resonance imaging (MRI) was used to assess lung tumor extent of TetO-KRASG12D transgenic mice.
2. Specify the number of blocks, trials or experimental units per session and/or subject, and specify the length of each trial or block (if trials are blocked) and interval between trials.	Not applicable
3. Describe how behavioral performance was measured.	Not applicable

Acquisition

4. Imaging	
a. Specify the type(s) of imaging.	Structural MRI
b. Specify the field strength (in Tesla).	7.0 Tesla
c. Provide the essential sequence imaging parameters.	T2_TurboRARE sequence: FOV = 30 × 30 mm, MTX = 256 × 256, SL = 1 mm, TE = 61.2 ms, TR = 2320 ms, and NEX = 4, ETL= 10, FA= 90.
d. For diffusion MRI, provide full details of imaging parameters.	Not applicable
5. State area of acquisition.	Axial planes thoracic cavity scan

Preprocessing

6. Describe the software used for preprocessing.	Not applicable
7. Normalization	
a. If data were normalized/standardized, describe the approach(es).	Not applicable
b. Describe the template used for normalization/ transformation.	Not applicable
8. Describe your procedure for artifact and structured noise removal.	Not applicable
9. Define your software and/or method and criteria for volume censoring, and state the extent of such censoring.	Not applicable

Statistical modeling & inference

10. Define your model type and settings.	Not applicable
11. Specify the precise effect tested.	Not applicable

Nature Biotechnology: doi:10.1038/nbt.4071

12. Analysis

a. Specify whether analysis is whole brain or ROI-based. Not applicable

b. If ROI-based, describe how anatomical locations were determined. Not applicable

13. State the statistic type for inference. (See Eklund et al. 2016.) Not applicable

14. Describe the type of correction and how it is obtained for multiple comparisons. Not applicable

15. Connectivity

a. For functional and/or effective connectivity, report the measures of dependence used and the model details. Not applicable

b. For graph analysis, report the dependent variable and functional connectivity measure. Not applicable

16. For multivariate modeling and predictive analysis, specify independent variables, features extraction and dimension reduction, model, training and evaluation metrics. Not applicable

Nature Biotechnology: doi:10.1038/nbt.4071